



RESEARCH ARTICLE | FEBRUARY 28 2024

Effects of interface model on performance of a vortex pump in CFD simulations ^{EP}

Wenguang Li  



International Journal of Fluid Engineering 1, 013901 (2024)

<https://doi.org/10.1063/5.0196213>



View
Online



Export
Citation

CrossMark



Editor's Pick

Effects of interface model on performance of a vortex pump in CFD simulations

Cite as: *Int. J. Fluid Eng.* **1**, 013901 (2024); doi: [10.1063/5.0196213](https://doi.org/10.1063/5.0196213)

Submitted: 5 January 2024 • Accepted: 4 February 2024 •

Published Online: 28 February 2024



View Online



Export Citation



CrossMark

Wenguang Li^{a)}

AFFILIATIONS

School of Mathematics and Statistics, University of Glasgow, Glasgow G12 8QQ, United Kingdom

^{a)} Author to whom correspondence should be addressed: wenguang.li@glasgow.ac.uk

ABSTRACT

That the predicted head of a vortex pump is higher than that measured experimentally is very common in simulations of turbulent flow in such pumps. To identify why, reported here is a study of the turbulent flow of water in a vortex pump with a specific speed of 76 and fluid domains with 1/8-impeller and whole-impeller geometrical models and smooth walls using the 3D steady Reynolds-averaged Navier–Stokes equations, the standard k - ϵ model, and a scalable wall function in ANSYS CFX 2019 R2. The results show that the aforementioned phenomenon is related to the choice of interface model. With the 1/8-impeller model, the head predicted by the frozen rotor model agrees with the experimental head. By contrast, the transient rotor model provides a reasonably accurate head against the experimental head but requires huge computing resources and overestimates the pump efficiency, and the stage model is unsuitable for predicting the head of the pump. The flow patterns in the vaneless chamber and impeller predicted with the 1/8-impeller model are more uniform because of artificial fluid mixing on the interface than those predicted with the whole-impeller model by using the frozen rotor model, and the flow patterns predicted with the whole-impeller model by using the transient rotor model are in between. The hydraulic performance of the pump is predicted with the 1/8-impeller model and frozen rotor model at various viscosities, and the flow-rate, head, and efficiency correction factors are determined and correlated with the impeller Reynolds number.

© 2024 Author(s). All article content, except where otherwise noted, is licensed under a Creative Commons Attribution (CC BY) license (<http://creativecommons.org/licenses/by/4.0/>). <https://doi.org/10.1063/5.0196213>

I. INTRODUCTION

A vortex pump (VP) is a rotodynamic pump that sucks fluid into a semi-open impeller from a vaneless side chamber and then discharges the fluid, thereby transmitting the mechanical energy of the impeller to the fluid. Because the fluid moves rotationally in the chamber, any solid matter in the fluid is carried away from the pump without blocking the impeller. This unique blockage-free feature gives VPs extensive applications for waste-water treatment and in the chemical, petro-chemical, food, and metallurgical industries.

Numerous studies have investigated the hydraulic performance and fluid mechanics of VPs experimentally. For example, how the impeller, volute, and suction pipe affected the hydraulic performance of a VP was examined in Refs. 1 and 2 with water as the flowing fluid. In Ref. 3, the hydraulic performance of a VP was measured with air as the flowing fluid; the hydraulic loss was analyzed,

and a flow model was proposed that comprised a through flow and a circulating flow in the VP. In Ref. 4, the hydraulic losses in a VP were modelled based on measurements of the fluid field between the impeller and side chamber. That model was verified experimentally in Refs. 5 and 6 and analytically in Ref. 7. In Ref. 8, the hydraulic performance of a VP was measured for various particle sizes and concentrations, and the patterns of particle erosion in the pump were visualized. In Ref. 9, measurements were made of the improved performance of a VP when the impeller was moved into the side chamber. In Ref. 10, the hydraulic and suction performances of a VP were measured when pumping rapeseeds, wheat grains, and soya beans at 6% volumetric concentration. In Refs. 11 and 12 the air–water two-phase flow in a VP was mapped by using probes. Furthermore, dilute salt crystal–water two-phase flow fields in the impeller^{13–15} and side chamber¹⁶ of a VP were measured by using particle image velocimetry. In Ref. 17, the hydraulic performance of a VP with different impeller diameter, number of blades, and

blade discharge angle was measured under non-woven textile–water two-phase flow conditions.

Numerical simulations have become increasingly vital for predicting the hydraulic performance of VPs and the details of the fluid flow therein. Initially, the 3D potential flow in the impeller of a VP was simulated by using the streamline curvature method¹⁸ and the boundary element method.¹⁹ Later, 3D, steady, incompressible, and turbulent single-phase flows in VPs were simulated using computational fluid dynamics (CFD).^{20–34} Also, numerical simulations have been performed of 3D steady turbulent solid–water^{35–38} fiber–water³⁹ and air–water^{40,41} two-phase flows. Furthermore, unsteady non-cavitating and cavitating water flows in a VP were simulated using Fluent in Ref. 42 and ANSYS CFX in Ref. 43. In Ref. 44, the vortex pattern in the side chamber of a VP was predicted using ANSYS CFX.

The present author has also conducted numerical simulations of the hydraulic performance of a VP and the flow therein^{45,46} and of a VP as a turbine.^{47–49} A critical issue that arose in those studies was that the predicted head of the VP was higher than the experimental value measured for water flow. Clearly, it is disappointing that the predicted head disagrees with the experimental measurement, and it suggests that the modelling procedure involved some improper treatment. Therefore, reported herein is a systematic investigation conducted using the CFD software ANSYS CFX 2019 R2 to resolve the issue, which it turns out is due to the choice of impeller geometrical model and interface model.

II. PUMP, FLOW DOMAIN, AND ISSUE UNDER INVESTIGATION

The hydraulic performance of the motor-connected VP (model 32WB8-12) studied herein has been measured under water single-phase flow conditions²⁴ and solid–water¹⁰ and air–water¹² two-phase flow conditions. This VP was used in CFD simulations^{45–49} to investigate how the liquid viscosity affects its hydraulic performance and fluid flow. The pump is shown schematically in cross section in Fig. 1(a), and its specifications and main geometrical dimensions are given in Table I.

As in the CFD simulations reported in Refs. 20–25 the axial symmetry of the suction pipe and impeller is ignored, and a complete fluid domain is generated as shown in Fig. 1(b). This comprises three individual fluid domains, i.e., the suction pipe, the impeller, and the volute, leading to a fluid–fluid interface at the boundary between the suction pipe and the impeller and another one at the boundary between the impeller and the volute. When these interfaces are crossed, the reference frame for the governing equations changes.

In each fluid domain, the fluid is incompressible, and its flow in the pump is three-dimensional and turbulent. The governing equations for the flow are the Reynolds-averaged Navier–Stokes equations in the multiple reference frame (MRF) setting. The continuity equation⁵⁰ is

$$\frac{\partial \rho}{\partial t} + \nabla \cdot [\rho(\vec{V} - \vec{\omega} \times \vec{r})] = 0, \quad (1)$$

and the momentum equation⁵⁰ is

$$\begin{aligned} \frac{\partial}{\partial t}(\rho \vec{V}) + \nabla \cdot [\rho(\vec{V} - \vec{\omega} \times \vec{r}) \vec{V}] + \rho[\vec{\omega} \times (\vec{V} - \vec{\omega} \times \vec{r})] \\ = -\nabla p + \nabla \cdot [(\mu + \mu_t)(\nabla \vec{V} + \nabla \vec{V}^T)], \end{aligned} \quad (2)$$

where we have $\vec{\omega} = \vec{e}_x \omega$ in the impeller but $\vec{\omega} = 0$ in the suction pipe and volute. Furthermore, \vec{e}_x is the unit vector of the x -coordinate aligned with the pump shaft axis, \vec{r} is the coordinate vector of fluid particles, \vec{V} is the fluid velocity vector, ρ is the fluid density, p is the fluid static pressure, μ is the fluid dynamic viscosity, and μ_t is the turbulent eddy viscosity.

The standard k – ε two-equation turbulence model is used to estimate the turbulent eddy viscosity μ_t , and the equations for k and ε ⁵⁰ are

$$\frac{\partial}{\partial t}(\rho k) + \nabla \cdot (\rho \vec{V} k) = \left[\left(\mu + \frac{\mu_t}{\sigma_k} \right) \nabla k \right] + G_k - \rho \varepsilon \quad (3)$$

and

$$\frac{\partial}{\partial t}(\rho \varepsilon) + \nabla \cdot (\rho \vec{V} \varepsilon) = \left[\left(\mu + \frac{\mu_t}{\sigma_\varepsilon} \right) \nabla \varepsilon \right] + \frac{\varepsilon}{k} (C_{1\varepsilon} G_k - C_{2\varepsilon} \rho \varepsilon), \quad (4)$$

where $\mu_t = \rho C_\mu k^2 / \varepsilon$, $G_k = \mu_t (\nabla \vec{V} + (\nabla \vec{V})^T) : \nabla \vec{V}$ describes the production of turbulent kinetic energy, and the constants $C_{1\varepsilon}$, $C_{2\varepsilon}$, C_μ , σ_k , and σ_ε are 1.44, 1.92, 0.09, 1.0, and 1.3, respectively.⁵⁰

The non-equilibrium wall function is used to calculate the wall shear stress τ_w by accounting for how the pressure gradient in the primary flow direction affects the shear stress dp/dL . The wall function⁵⁰ is

$$\begin{aligned} \left\{ u_c - \frac{1}{2} \frac{dp}{dL} \left[\frac{y_v}{\rho \kappa k^{1/2}} \ln \left(\frac{y}{y_v} \right) + \frac{y - y_v}{\rho \kappa k^{1/2}} + \frac{y_v^2}{\mu} \right] \right\} \frac{C_\mu^{1/4} k^{1/2}}{\tau_w / \rho} \\ = \frac{1}{\kappa} \ln \left(\frac{E \rho C_\mu^{1/4} k^{1/2} y}{\mu} \right) \end{aligned} \quad (5)$$

where u_c is the fluid velocity in the primary/core flow direction, E is the turbulence constant, y_v is the viscous sublayer thickness of the boundary layer, dp/dL is the pressure gradient in the primary flow direction L , κ is the von Kármán constant, and y is the perpendicular distance between a mesh node and the nearest wall.

The finite volume method is used to discretize Eqs. (1)–(4). Pressure–velocity coupling is accomplished using the SIMPLE algorithm; the pressure and velocity are assigned in a staggered mesh, which is the PRESTO scheme in Fluent 6.3. The second-order upwind scheme is selected for the advective terms in Eqs. (2)–(4), but the central difference scheme is selected for the dissipation terms in those equations.

At the entrance of the suction pipe, the velocity-inlet boundary condition is imposed with an axial velocity, 5% turbulence intensity, and 32-mm hydraulic diameter. The imposed axial velocity is calculated from the specified flow rate and the cross-sectional area of the pipe. At the volute nozzle outlet, a relative static pressure is specified along with 5% turbulence intensity and 23-mm hydraulic diameter. For the walls along which the flow passes, the no-slip boundary condition is imposed with zero roughness.

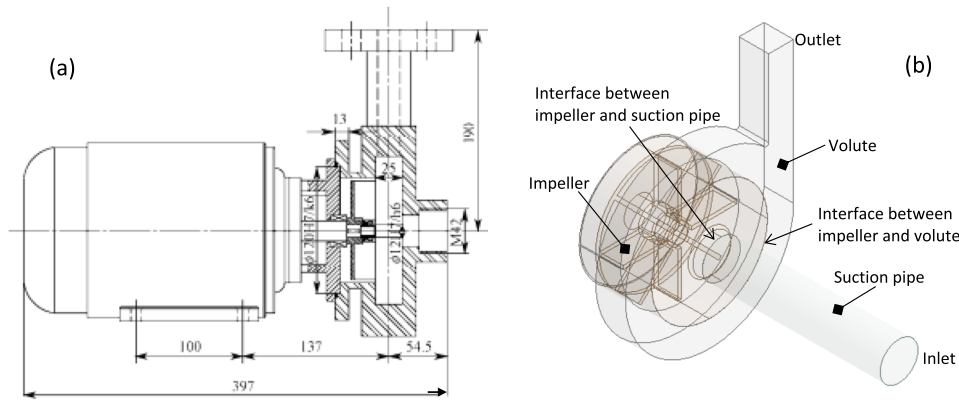


FIG. 1. (a) Cross-sectional drawing of vortex pump (VP) studied in Refs. 10 and 24 and (b) corresponding fluid domains generated for CFD simulations.

The under-relaxation coefficients for the pressure–velocity coupling equation, the momentum equation, and the equations for the turbulent kinetic energy and its dissipation are 0.3, 0.5, 0.8, and 0.8, respectively. The convergence criterion is 1×10^{-5} for the residuals of those equations.

The working liquids are water and five different machine oils, and their densities and kinematic viscosities are given in Table II along with the corresponding impeller Reynolds number. Oils 1–5 are 10#, 22#, 32#, 68#, and 100# mineral oils, respectively; the number before the “#.” is the kinematic viscosity at 40 °C in centistokes ($1 \times 10^{-6} \text{ m}^2/\text{s}$ or $1 \text{ mm}^2/\text{s}$) based on ISO 3448. These viscous oils are used only to study how viscosity affects the hydraulic performance of the VP.

The meshing software Gambit is used to generate three meshes, referred to as meshes 1–3. The mesh in the suction-pipe fluid domain is hexahedral, whereas those in the impeller and volute fluid domains are hybrid (tetrahedral near walls and interfaces but cubic in the core flow). The mesh information is summarized in Table III along with the mean dimensionless wall distance of mesh 2 at the best-efficiency point (BEP) ($Q = 8 \text{ m}^3/\text{h}$) and $\nu = 1 \text{ cSt}$. Fig. 2 shows the predicted hydraulic performance curves of the VP with the three meshes at $\nu = 1 \text{ cSt}$ in the MRF system in comparison with the experimental data from Ref. 24.

In Fig. 2, the efficiency shows some agreement between prediction and experiment, but the predicted head and shaft power are higher than the experimental data. Specifically, the errors in the head and shaft power are 6.92%–12.4% and 8.39%–14.8%, respectively, depending on the operational conditions, while the error in the efficiency is only between –1.01% and 1.57%, see Table IV.

This phenomenon was observed in Refs. 45–49 and why the predicted head is higher than the experimental data is clarified in Sec. III.

III. EFFECTS DUE TO GEOMETRICAL INTERFACE MODEL

A. Effect of y^+ value

From the outset, it is doubted that the y^+ value is responsible for the predicted head being higher than the experimental data, this

being because the y^+ value is related to the wall shear stress. A turbulent boundary layer near a smooth wall has an outer layer and an inner layer that are separated at ca. $y^+ = 350$; see Fig. 3(a). The velocity profile in the outer layer depends on the dimensionless pressure gradient and yields the velocity-defect law⁵¹ which can be handled with a turbulence model. The inner layer consists of an overlap layer ($30 \leq y^+ \leq 350$), a buffer layer ($5 \leq y^+ \leq 30$), and a viscous sublayer ($0 < y^+ \leq 5$).⁵¹ The velocity profile in the overlap layer of a turbulent boundary layer either with or without a pressure gradient is described by the logarithmic or exponential law⁵¹ i.e.,

$$u^+ = \frac{1}{\kappa} \ln y^+ + B \text{ or } y^+ = e^{\kappa(u^+ - B)}, \quad (6)$$

where κ is the von Kármán constant and B is the intercept of u^+ at $y^+ = 1$; smooth-pipe turbulent flow measurements by Nikuradse⁵¹ give $\kappa = 0.40$ and $B = 5.5$. In the buffer layer, the velocity profile is fitted with a single composite formula proposed by Spalding⁵¹ i.e.,

$$y^+ = u^+ + e^{\kappa(u^+ - B)} - e^{-\kappa B} \left[1 + \kappa u^+ + \frac{(\kappa u^+)^2}{2} + \frac{(\kappa u^+)^3}{6} \right]. \quad (7)$$

In fact, Eq. (7) fits the u^+ experimental data well in the range of $1 \leq y^+ \leq 350$ as shown in Fig. 3.

In the viscous sublayer, the relationship between y^+ and u^+ is linear⁵¹ i.e.,

$$y^+ = u^+. \quad (8)$$

Fluent and ANSYS CFX neglect the buffer layer but not the overlap layer and viscous sublayer (depending on the choice of turbulence model), and these are modelled with a wall function. For the k – ϵ two-equation model, a scalable wall function is proposed based on the empirical velocity scale u^* and a minimal y^+ ⁵² i.e.,

$$\tau_w = \rho u^* u_\tau, u^* = \max \left(C_\mu^{1/4} k^{1/2}, 0.01u/y^+ \right), \quad (9)$$

$$u_\tau = \frac{u}{\frac{1}{\kappa} \ln y^+ + B}, y^+ = \max \left(\frac{u^* \Delta y / 4}{\nu}, 11.06 \right)$$

TABLE I. Pump specifications and main geometrical parameters.

Classification	Parameter/type	Value/shape
Design conditions	Flow rate Q (m ³ /h)	8
	Head H (m)	12
	Rotational speed n (rpm)	2850
	Specific speed n_s^a	76
Impeller hydraulic dimensions	Impeller diameter d_2 (m)	96
	Blade shape	Radial, straight
	Blade span b (mm)	20
	Blade mate thickness (mm)	1.5
	Number of blades Z	8
Volute hydraulic dimensions	Volute shape	Concentric
	Width (mm)	25
	Base circle diameter (mm)	100
	Volute diameter (mm)	140
Pump inlet and outlet dimensions	Inlet diameter (mm)	32
	Outlet size (mm)	24 × 21

^a $n_s = \frac{3.65n\sqrt{Q}}{H^{\frac{3}{4}}}$ for n (rpm), Q (m³/s), and H (m).

TABLE II. Densities and kinematic viscosities of water and machine oils at 20 °C. Notes: $Re = \pi n d_2^2 / 120 \nu$, n is the impeller rotational speed (rpm), d_2 is the impeller diameter (m), ν is the liquid kinematic viscosity (mm²/s), and ρ is the liquid density.

Liquid	Water	Oil 1	Oil 2	Oil 3	Oil 4	Oil 5
ρ (kg/m ³)	1000	839	851	858	861	865
ν (cSt or mm ² /s)	1	24	48	60	90	120
Re	6.8763×10^5	2.8651×10^4	1.4326×10^4	1.1461×10^4	7.6404×10^3	5.7303×10^3

TABLE III. Mesh details and corresponding y^+ values. Notes: y^+ -dimensionless wall distance, $y^+ = u_\tau y_n / \nu$ is the dimensionless wall distance, $u_\tau = \sqrt{\tau_w / \rho}$ is the friction velocity at the nearest wall, and y_n is the mesh node distance to the nearest wall.

Mesh	Domain	Type	Number of cells	y^+ at BEP ($Q = 8$ m ³ /h)
Mesh 1	Suction pipe	Hexahedral	26 574	
	Impeller	Hybrid	419 209	N/A
	Volute		310 298	
	Total number of cells		756 081	
Mesh 2	Suction pipe	Hexahedral	43 430	427
	Impeller	Hybrid	543 355	97
	Volute		406 303	167
	Total number of cells		993 088	N/A
Mesh 3	Suction pipe	Hexahedral	80 520	
	Impeller	Hybrid	653 775	N/A
	Volute		581 016	
	Total number of cells		1 315 311	

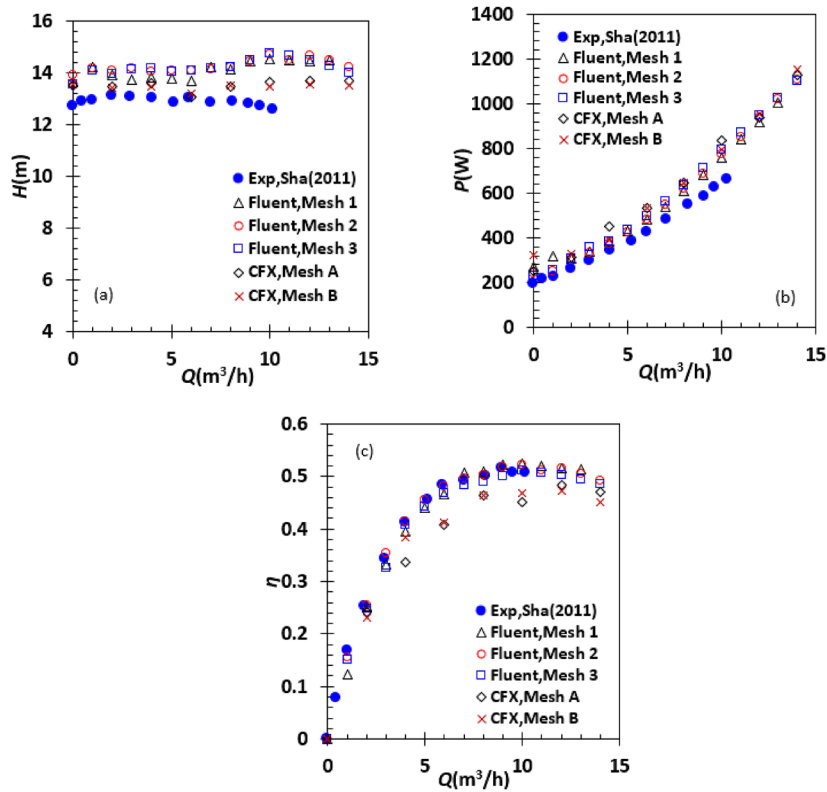


FIG. 2. Hydraulic performance curves predicted using Fluent 6.3 with multiple reference frame (MRF) setting and ANSYS CFX with frozen rotor model (FRM) at $\nu = 1$ cSt, and experimental data from Ref. 24: (a) head; (b) shaft power; (c) efficiency.

TABLE IV. Predicted head, shaft power, and efficiency in comparison with corresponding experimental data at part-load point and best-efficiency point (BEP). Note: the error in the head and shaft power is the relative error as a percentage, whereas the error in the efficiency is the absolute error as a percentage.

Condition	Performance	Mesh 1 (error)	Mesh 2 (error)	Mesh 3 (error)	Data (Ref. 24)
Part-load point, $Q = 4 \text{ m}^3/\text{h}$	H (m)	13.9(6.92%)	14.1(8.07%)	14.2(8.99%)	13.0
	P (W)	373.5(8.47%)	373.2(8.39%)	382.9(11.2%)	344.3
	η (%)	40.9(-0.27%)	41.5(0.37%)	40.8(-0.36%)	41.2
BEP, $Q = 8 \text{ m}^3/\text{h}$	H (m)	14.5(12.4%)	14.3(10.5%)	14.2(10.4%)	12.9
	P (W)	616.4(11.1%)	622.7(12.2%)	637.3(14.8%)	555.0
	η (%)	51.6(1.57%)	50.3(0.2%)	49.1(-1.01%)	50.1

where the function “max” selects the maximum from the variables given to it, Δy is the near-wall grid spacing, and the constant 11.06 is the minimal y^+ , which is the intersection point of the linear law in Eq. (9) and the logarithmic law in Eq. (6) with $\kappa = 0.41$ and $B = 5.2$ as suggest by Coles and Hirst.⁵¹ The scalable wall function can be used on arbitrarily fine meshes but cannot improve the computational accuracy on rough meshes in comparison with the wall function in Eq. (5).⁵²

From Table III, the mean y^+ values are close to or higher than 100 at the BEP, especially for the suction-pipe wall. Because Gambit cannot create an inflation boundary-layer mesh for a hybrid mesh, the complete fluid domain is read into ANSYS CFX and re-meshed using the ANSYS meshing module to generate an unstructured mesh with an inflation boundary-layer mesh near the wall to reduce the mean y^+ values. Figure 2 shows the hydraulic performance curves of the pump predicted using the frozen-rotor interface

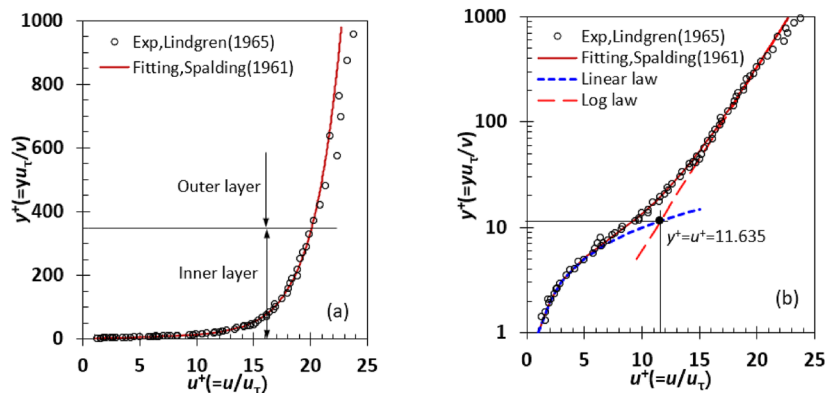


FIG. 3. Experimental and fitted dimensionless velocity profiles across a turbulent boundary layer: (a) linear $y^+ - u^+$ plot; (b) semi-logarithmic $y^+ - u^+$ plot. Here, $y^+ = u_\tau y / \nu$ and $u^+ = u / u_\tau$, where u is the fluid streamwise velocity in the boundary layer. The experimental data are from Ref. 51.

model (identical to MRF in Fluent) with two meshes, i.e., mesh A (3 430 427 cells) and mesh B (5 283 082 cells); see Table V for full details about these meshes. For mesh A, the mean y^+ values are 13.46–27.73 on the blades, 53.35–65.81 on the volute wall, 55.35–52.38 on the chamber wall, 24.37–35.79 on the impeller inside and outside surfaces, and 7.19–29.08 on the suction-pipe wall. For mesh B, even smaller mean y^+ values are observed. These values are much smaller than the counterparts of the meshes in Fluent 6.3 listed in Table III. The smaller mean y^+ values do reduce the head to make it closer to the experimental data, but they are not effective at the over-load point. The efficiency predicted with the smaller mean y^+ values is significantly lower than that with the larger mean y^+ values. These facts imply that the y^+ value is not fully responsible for the predicted head being higher than the experimental data.

B. Effect of choice of interface model

In ANSYS CFX, the computational domains can comprise fluid, solid, and porous domains depending on the problem to be solved. There is a domain interface between any two domains contacting each other, and there are six interface types, i.e., fluid–fluid, fluid–porous, fluid–solid, porous–porous, solid–porous, and solid–solid. However, for isothermal fluid flows in hydro-turbomachinery, the domain interface type is fluid–fluid.⁵³ The interface model specifies how the solver models physical processes across the interface. ANSYS CFX has two types of interface model, i.e., periodical connection and general grid connection. Periodical connection involves translational periodicity and rotational periodicity, while general grid connection involves grid connection and reference-frame change among the frozen rotor model (FRM), stage model (SM), and transient rotor model (TRM).⁵³ A detailed interface-model tree is shown in Fig. 4.

Periodical connection is a grid connection between a pair of symmetric or axisymmetric edges/planes/surfaces in 2D or 3D space. When fluid crosses a pair of symmetric or axisymmetric geometrical elements, the fluid velocity or heat flux remains unchanged. General grid connection includes grid connection either with or without

reference-frame change; in the former case, a stationary reference frame changes into a rotational reference frame or vice vs, or from one rotational reference frame to another with different rotational angular speeds.

In the FRM, even though the reference frame changes across the interface, the relative orientation of the two fluid domains remains fixed across the interface. If the pitch of the two fluid domains varies across the interface, then the fluid flow parameters are scaled by the pitch change. The FRM is equivalent to the MRF model in Fluent, and it produces a steady solution by taking account of the interaction between rotor and stator to some degree with minimal computational time. However, the mixing loss between rotor and stator is ignored.

In the SM, the relative position between rotor and stator is not fixed, and circumferential averaging is performed to ensure that the fluxes of fluid variables on both sides of an interface are conserved; as a result, steady solutions are produced in each reference frame. This circumferential averaging at the interface induces a mixing loss that is equivalent to real fluid mixing taking place at the interface to some degree. The SM accounts for time-averaged interaction effects between rotor and stator but ignores transient interaction effects. Furthermore, the SM is not suitable for a rotodynamic pump with a volute in off-design conditions where the fluid variables vary markedly in the circumferential direction. In the circumferential averaging, a constraint can be applied to the total pressure or velocity.

In the TRM, the motion of the rotor relative to the stator varies with each timestep, and the transient interaction of the flow between the stator and the rotor is predicted. The TRM uses the flow field predicted by the FRM or SM as the initial flow field and is quite time-consuming in comparison with those two models. The TRM in ANSYS CFX is the same as the sliding mesh model in Fluent.

To clarify how the choice of interface model affects the performance of the VP, periodical connection and the FRM, SM, and TRM are adopted here. Because the impeller has eight repeated flow passages, just one is chosen in the impeller fluid domain, and thus only 1/8 sectors of the casing chamber and suction pipe are included in the fluid domain as shown in Fig. 5. The pitches of the interface

TABLE V. Details of two meshes used in ANSYS CFX simulations of fluid domains shown in Fig. 1. Notes: Tet4—four-node tetrahedral element; Wed6—six-node wedge element; $y^+ = y_n u_\tau / \nu$ —dimensionless wall distance, y_n —distance of a mesh node from nearest wall, u_τ —friction velocity of fluid at nearest wall, ν —kinematic viscosity of fluid.

Item		Mesh A	Mesh B
Element size (mm)		1.5	1
Number of nodes		1 174 025	1 753 399
Number of elements	Total	3 430 427	5 283 082
	Tet4	2 053 339 (59.8%)	3 194 050 (60.5%)
	Wed6	1 368 213 (39.9%)	2 083 276 (39.4%)
	Pyr5	8875 (0.3%)	5756 (0.1%)
Element quality		0.6892 ± 0.2426	0.6588 ± 0.2713
Aspect ratio		3.2097 ± 2.8762	3.7933 ± 3.6477
Skewness		0.2423 ± 0.1393	0.2292 ± 0.1347
Orthogonal quality		0.7568 ± 0.1383	0.7698 ± 0.1336
Pipe		0.125	0.125
Volute		0.125	0.075
Blade, hub, front casing		0.125	0.075
Top casing		1 (maximum boundary layer thickness)	
Rear casing		0.125	0.075
Pipe		8	
Volute		8	
Blade, hub, front casing		5	
Top casing		4	
Rear casing		5	
Pipe		1.2	
Volute		1.2	
Blade, hub, front casing		1.2	
Top casing		1.2	
Pipe		1.2	
Blade		13.46–27.73	9.00–17.89
Casing		55.35–52.38	30.94–27.02
Impeller inside and outside surface		24.37–35.79	14.93–21.45
Pipe		7.19–29.08	6.76–29.37
Volute		53.35–65.81	42.94–50.69

between the suction pipe and the impeller are equal, but those of the interface between the volute and the impeller are different with an 8:1 (volute to impeller) pitch ratio. There is a periodical connection between the two periodical surfaces in the impeller and suction-pipe fluid domains.

First, the mesh size independence is checked with the FRM, and details of the four unstructured meshes used for this purpose, i.e., meshes I–IV, in which six-node wedge elements are dominant, are listed in Table VI. Inflation mesh layers are arranged on the walls of the suction pipe, volute, blade, hub, and chamber to handle the fluid flow in the boundary layers over them. Except for meshes I and II, the dimensionless wall distance y^+ is smaller than 13, and the scalable wall function in Eq. (9) is basically satisfied.

In Fig. 6, the head H_{BEP} , shaft power P_{BEP} , and overall efficiency η_{BEP} at the BEP ($Q_{BEP} = 8 \text{ m}^3/\text{h}$) are plotted against the number of mesh elements under water flow conditions. As can be seen, η_{BEP}

remains almost constant with the number of mesh elements from mesh III to mesh IV, so mesh size independence is achieved with meshes III and IV.

Second, the performance curves of the VP are predicted using ANSYS CFX based on the fluid domains shown in Fig. 5 and the FRM, and these are compared in Fig. 7 with the experimental data from Ref. 24. The head curves predicted with the four meshes exhibit much better agreement with the experimental data than do those in Fig. 2 predicted with the FRM and the fluid domains shown in Fig. 1. For example, the mean errors in the head in Fig. 7 are 2.79% and 0.53% compared with the errors of 7.99% and 11.09% in the head in Fig. 2, against the measured head data at the part-load point ($Q = 4 \text{ m}^3/\text{h}$) and the BEP ($Q_{BEP} = 8 \text{ m}^3/\text{h}$), respectively.

The shaft power and efficiency curves predicted with the fluid domains in Fig. 5 and the FRM are slightly poorer in agreement with the experimental data than are those in Fig. 2. The mean errors in

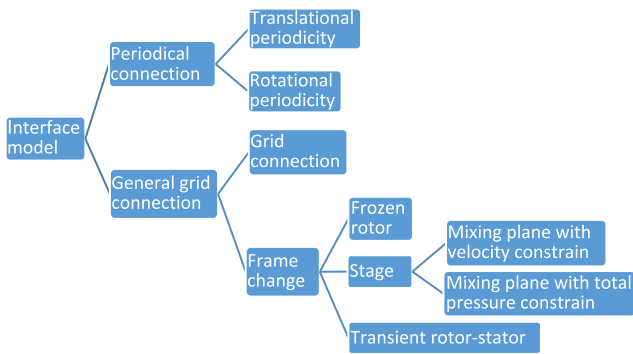


FIG. 4. Interface models in ANSYS CFX.

the shaft power are 18.17% and 6.66% in Fig. 7 against the measured data in comparison with the errors of 9.35% and 12.30% in Fig. 2 at the part-load point ($Q = 4 \text{ m}^3/\text{h}$) and the BEP ($Q_{BEP} = 8 \text{ m}^3/\text{h}$), respectively. Regarding the overall efficiency, the errors are -4.25% and -1.39% in Fig. 7 compared with -0.09% and 0.25% in Fig. 2. at the two operative points, respectively. Note that the shaft power in Ref. 24 was calculated from the electrical power consumed by the electrical motor and its efficiency. However, the rated efficiency was obtained from the product catalogue of the motor manufacturer and so was not sufficiently accurate, causing the experimental shaft power as well as the efficiency calculated in Ref. 24 to have large errors when compared with the experimental head and flow rate.

Third, how the choice of interface model affects the hydraulic performance curves of the VP is clarified. The head, shaft power, and efficiency predicted with the fluid domains in Fig. 5 and the FRM, SM, and TRM are shown in Fig. 8 for mesh III and water. Compared with the FRM, the SM leads to a significantly low head and

small shaft power as well as poor efficiency against the corresponding experimental data. The TRM results in a slightly lower head and shaft power but a higher efficiency. The head predicted using the TRM agrees well with that estimated using the FRM except at $Q = 2$ and $4 \text{ m}^3/\text{h}$. However, the shaft power predicted with the former is considerably lower than that given by the latter and is closer to the experimental data.

Based on the head predicted by using the FRM, SM, and TRM in the fluid domains with periodical connection, the FRM and TRM are more suitable for predicting the hydraulic performance of the VP than is the SM. However, the TRM requires much more computational resources than does the FRM and so is limited in applications. Therefore, unless unsteady turbulent flow is happening in the VP, the FRM is recommended as the best interface model for predicting the pump performance.

IV. EFFECTS OF VISCOSITY ON PERFORMANCE

A. Performance curves

Figure 9 shows the hydraulic performance curves of the VP for kinematic viscosity $\nu = 1, 24, 48, 60, 90,$ and 120 cSt and the corresponding densities in Table II as predicted using the FRM and the fluid domains with periodical connection shown in Fig. 5. Even though the disc friction power is not a parameter of the hydraulic performance, it can affect the shaft power greatly at high viscosity and so was extracted from the ANSYS CFX result files and is also shown in Fig. 9.

Generally, the head, efficiency, and disc friction power rise with increasing kinematic viscosity but are insensitive to density at a given flow rate. The shaft power depends on kinematic viscosity, density, and flow rate. At zero flow rate, the shaft power depends on kinematic viscosity. With increasing flow rate, the shaft power is increasingly affected by density but is decreasingly influenced by kinematic viscosity; i.e., the denser and thicker the fluid, the greater the shaft power.

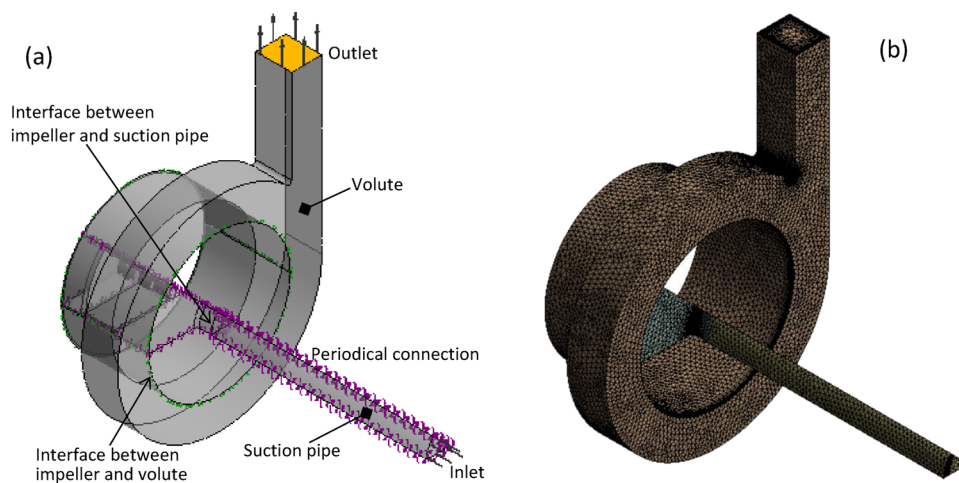


FIG. 5. (a) Fluid domains comprising whole volute, 1/8 flow passage, and 1/8 sector of suction pipe, and (b) mesh structure.

TABLE VI. Details of four meshes used in ANSYS CFX simulations of fluid domains shown in Fig. 5. Notes: Tet4—four-node tetrahedral element; Wed6—six-node wedge element; y^+ = $y_n \mu_r / \nu$ —dimensionless wall distance; y_r —distance of a mesh node from nearest wall; u_r —friction velocity of fluid at nearest wall; ν —kinematic viscosity of fluid.

Item	Mesh I	Mesh II	Mesh III	Mesh IV
Element size (mm)	1.5	1.25	1.05	0.875
Number of nodes	345 266	533 858	790 027	1 131 778
Total	915 157	1 390 619	2 024 725	2 918 097
Tet4	409 885 (44.8%)	586 537 (42.2%)	811 038 (40.0%)	1 182 241 (40.5%)
Wed6	49 9403 (54.6%)	796 134 (57.2%)	1 208 439 (59.7%)	1 731 641 (59.3%)
Pyr5	5869 (0.6%)	7948 (0.6%)	5248 (0.3%)	4215 (0.2%)
Element quality	0.4305 ± 0.3619	0.4216 ± 0.3532	0.4210 ± 0.3463	0.4420 ± 0.3371
Aspect ratio	16.74 ± 21.74	15.46 ± 19.54	13.27 ± 14.50	11.09 ± 11.97
Skewness	0.2561 ± 0.1609	0.2572 ± 0.1646	0.2271 ± 0.1391	0.2208 ± 0.1362
Orthogonal quality	0.7382 ± 0.1685	0.7350 ± 0.1745	0.7696 ± 0.1426	0.7772 ± 0.1377
Pipe		0.05		
Volute		0.025		
Blade, hub, front casing		0.025		
Top casing		0.025		
Rear casing		0.025		
Pipe		12		
Volute		14		
Blade, hub, front casing		12		
Top casing		6		
Rear casing		12		
Pipe		1.2		
Volute				
Blade, hub, front casing				
Top casing				
Pipe				
Blade	4.29–7.51	6.45–13.19	3.27–6.69	3.44–6.90
Front casing	13.03–12.44	25.13–26.02	13.01–12.52	12.90–12.55
Rear casing	6.21–3.27	6.56–3.13	6.57–3.09	6.52–3.11
Impeller outside surface	6.54–8.68	6.62–8.86	6.63–8.86	6.65–8.92
Impeller inside surface	3.08–7.98	4.83–13.20	2.48–6.34	2.74–6.57
Pipe	4.90–11.72	5.30–11.77	4.99–11.78	4.97–11.78
Volute	42.67–45.06	11.19–12.74	10.33–12.16	10.52–11.94

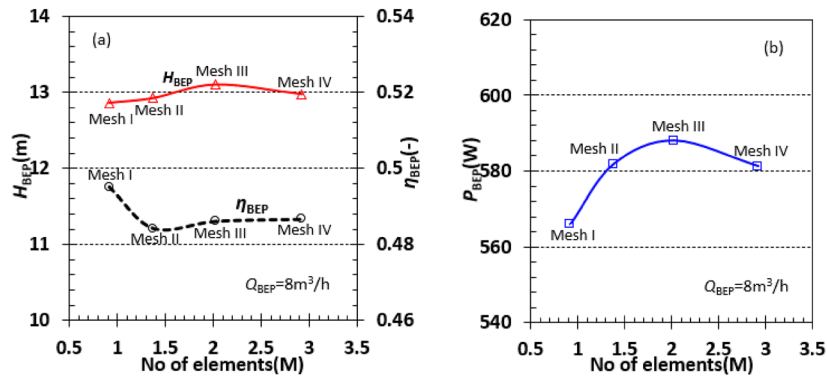


FIG. 6. (a) Head H_{BEP} , (b) shaft power P_{BEP} , and (c) efficiency η_{BEP} plotted against number of elements in meshes I–IV at BEP flow rate Q_{BEP} for water. The number of elements M is given in millions.

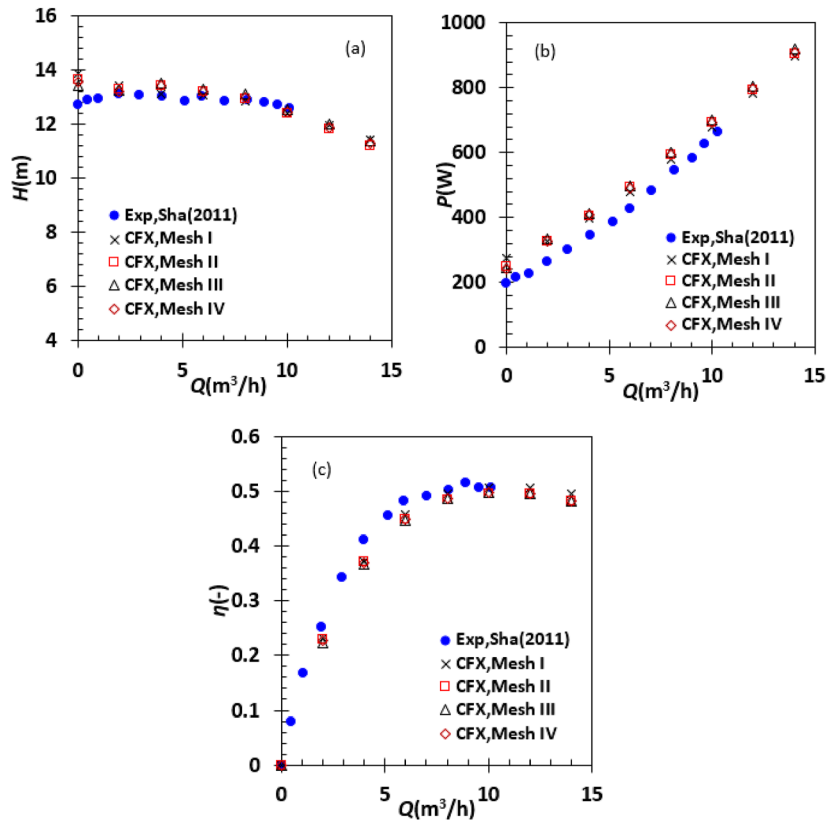


FIG. 7. Performance curves of VP predicted using ANSYS CFX with four meshes based on fluid domains shown in Fig. 5(a) and FRM for water: (a) head H ; (b) shaft power P ; (c) efficiency η . Exp—experimental data from Ref. 24.

B. Correction factors

The correction factors are the ratios of the flow rate, head, and efficiency of the VP at a given kinematic viscosity to those at the viscosity of water at 20°C at a few operational points. Based on the

correction factors, the performance curves at any viscosity can be calculated from those at the viscosity of water at 20°C . The correction factors k_Q , k_H , and k_η of flow rate, head, and efficiency at the operational points of 0.6BEP, BEP, and 1.2BEP are defined as follows:

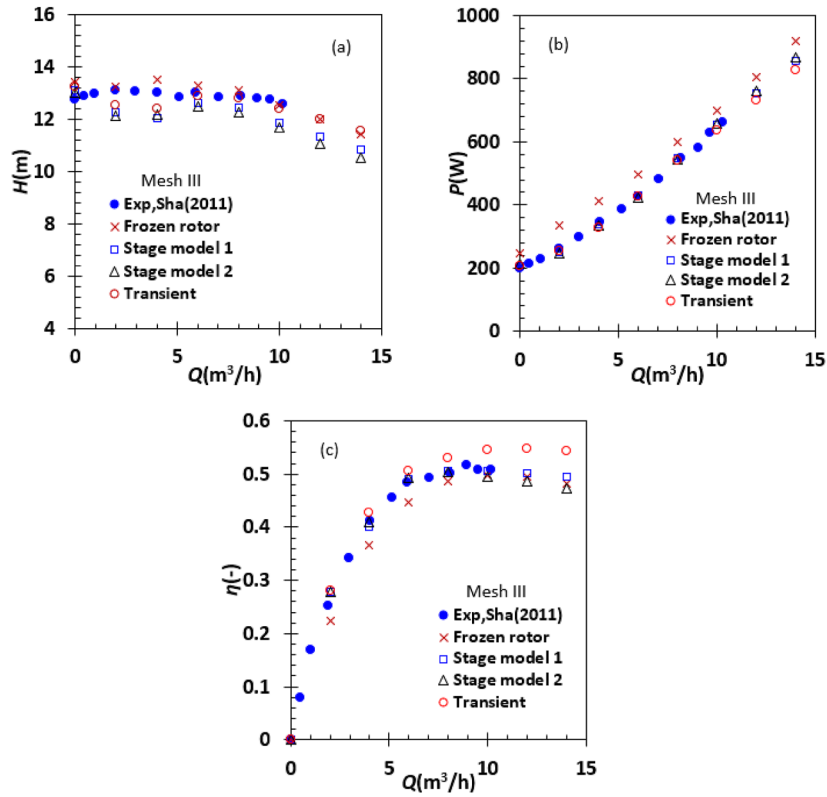


FIG. 8. (a) Head, (b) shaft power, and (c) efficiency predicted using fluid domains in Fig. 5(a) and FRM, stage model (SM), and transient rotor model (TRM) with mesh III and water. SM 1 constrains the total pressure downstream, whereas SM 2 constrains the average velocity downstream.

$$\begin{cases} k_Q = \frac{Q}{Q_w} \text{ at } 0.6\text{BEP, BEP, and } 1.2\text{BEP,} \\ k_H = \frac{H}{H_w} \text{ at } 0.6\text{BEP, BEP, and } 1.2\text{BEP,} \\ k_\eta = \frac{\eta}{\eta_w} \text{ at } 0.6\text{BEP, BEP, and } 1.2\text{BEP,} \end{cases} \quad (10)$$

where Q , H , and η are the pump flow rate, head, and efficiency at any viscosity, and Q_w , H_w , and η_w are those at the viscosity of water at 20°C at 0.6BEP, BEP, and 1.2BEP. Based on the performance curves in Fig. 9, the correction factors are determined at 0.6BEP, BEP, and 1.2BEP and are plotted vs the impeller Reynolds number Re in Fig. 10. The correlation equation for the flow-rate correction factor is

$$k_Q = 1.1630 - 0.1630 \left(\frac{Re}{Re_w} \right)^{0.08} \text{ at } 0.6\text{BEP, BEP, and } 1.2\text{BEP,} \quad (11)$$

those for the head correction factor are

$$k_H = \begin{cases} 1.0415 - 0.0437 \left(\frac{Re}{Re_w} \right)^{-0.3} & \text{at } 0.6\text{BEP,} \\ 1.0558 - 0.0561 \left(\frac{Re}{Re_w} \right)^{-0.3} & \text{at BEP,} \\ 1.0635 - 0.0628 \left(\frac{Re}{Re_w} \right)^{-0.3} & \text{at } 1.2\text{BEP,} \end{cases} \quad (12)$$

and those for the efficiency correction factor are

$$k_\eta = \begin{cases} 1.2326 - 0.2338 \left(\frac{Re}{Re_w} \right)^{-0.16} & \text{at } 0.6\text{BEP,} \\ 1.2474 - 0.2485 \left(\frac{Re}{Re_w} \right)^{-0.16} & \text{at BEP,} \\ 1.2512 - 0.2502 \left(\frac{Re}{Re_w} \right)^{-0.16} & \text{at } 1.2\text{BEP.} \end{cases} \quad (13)$$

As shown in Fig. 10, k_Q is identical at 0.6BEP, BEP, and 1.2BEP and increases slightly with decreasing Re , whereas k_H and k_η decrease with decreasing Re . For given Re , we have $k_Q \geq k_H \geq k_\eta$, and the operational condition influences k_H more substantially than it influences k_η .

Figure 11, k_Q , k_H , and k_η of the VP are compared with the correction factors of centrifugal pumps with a closed impeller in Ref. 54 ($n_s = 92$), Refs. 55 and 56 ($n_s = 47$), and Ref. 57 ($n_s = 107$) and with a semi-open impeller in Ref. 58 ($n_s = 121$, 1-mm blade side-tip gap) at BEP based on the measured performance curves and the correction factors predicted by using the empirical correlations of KSB (a notable pump manufacturer) and the American Hydraulic Institute presented in Ref. 59. As can be seen, the correction factors of the VP differ significantly from the other factors.

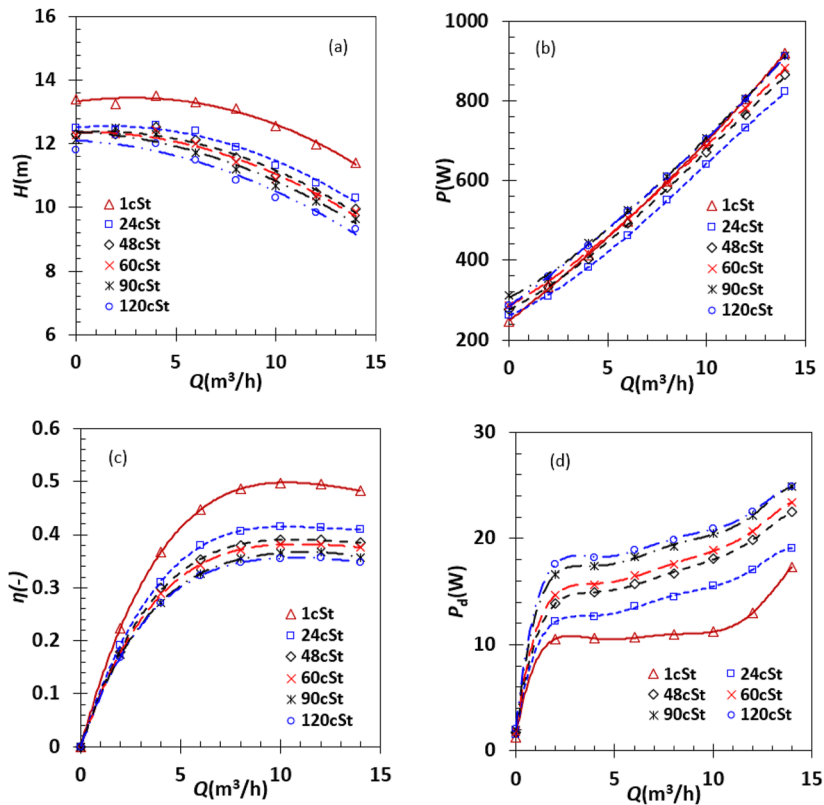


FIG. 9. Hydraulic performance curves of VP predicted using FRM and fluid domains with periodical connection for kinematic viscosity $\nu = 1$ cSt, 24 cSt, 48 cSt, 60 cSt, 90 cSt, and 120 cSt: (a) head; (b) shaft power; (c) efficiency; (d) disc friction loss power.

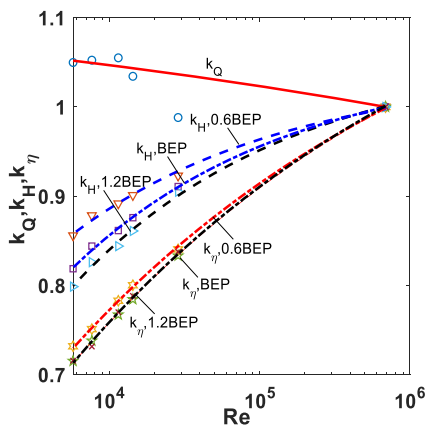


FIG. 10. Correction factors k_Q , k_H , and k_η for flow rate, head, and efficiency of VP at 0.6BEP, BEP, and 1.2BEP.

Basically, k_Q and k_η of the VP are larger but k_H is smaller than the counterparts of the centrifugal pumps based on the experimental data at given Re. The same is true for k_Q and k_η of the VP in

comparison with those estimated by the empirical correlations for centrifugal pumps, but k_H is comparable between the two types of pump. Therefore, the head of the VP is influenced more strongly by viscosity than is that of centrifugal pumps. The efficiency of the VP is reduced less by viscosity than is that of centrifugal pumps, while the flow rate of the VP is least affected by viscosity compared with centrifugal pumps.

In Fig. 12(a), the efficiency of the VP at BEP is compared with those of the centrifugal pumps reported in Refs. 55–61. The impellers of the centrifugal pumps in Refs. 55–57, 60 were closed, but those in Refs. 58 and 61 ($n_s = 85$) were semi-open. The efficiency of the centrifugal pumps with a closed impeller suffers from substantial incremental loss with increasing viscosity (decreasing Re) compared with the pumps with a semi-open impeller. The efficiency of the VP decreases less rapidly with increasing viscosity than does that of the centrifugal pumps with a semi-open impeller, and this is due to the smaller disc friction loss power in the VP.

The ratio P_d/P of the impeller disc friction loss power to the shaft power is calculated for the VP and correlated with the impeller Reynolds number, and the corresponding correlations are

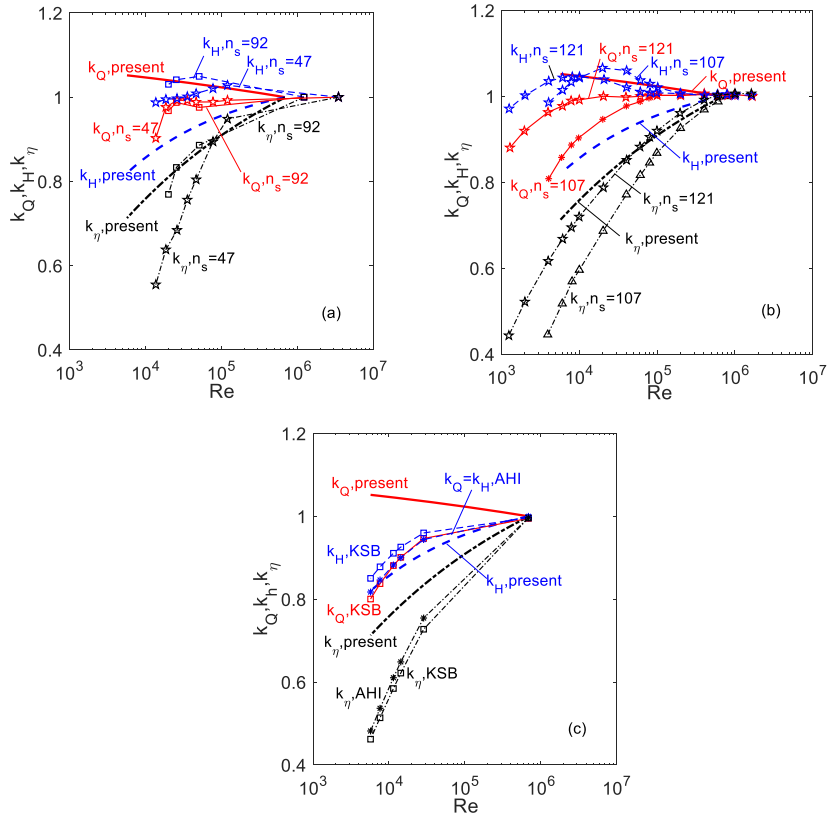


FIG. 11. Comparison of three correction factors of VP at BEP with those based on measured hydraulic performance curves and predicted with existing empirical correlations for centrifugal pumps: (a) results for centrifugal pumps with closed impeller in Ref. 54 ($n_s = 92$) and Refs. 55 and 56 ($n_s = 47$); (b) results for centrifugal pumps with closed impeller in Ref. 57 ($n_s = 107$) and semi-open impeller in Ref. 58 ($n_s = 121$, 1-mm blade side-tip gap); (c) correction factors predicted by empirical correlations proposed by KSB (a pump manufacturer) and the American Hydraulic Institute in Ref. 59.

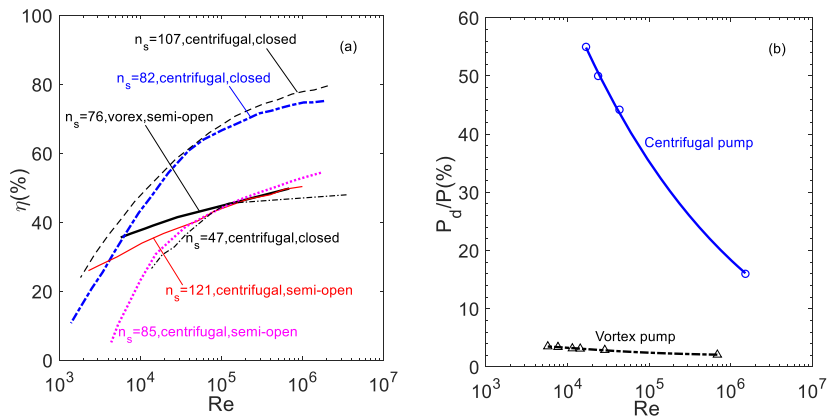


FIG. 12. Efficiency of VP and centrifugal pumps at BEP and ratio of disc friction loss power to shaft power plotted against impeller Reynolds number: (a) efficiency; (b) P_d/P . The centrifugal pumps in Ref. 58 ($n_s = 121$) and 61 ($n_s = 85$) had a semi-open impeller, but those in Refs. 55–57, 60 had a closed impeller.

29 February 2024 10:33:02

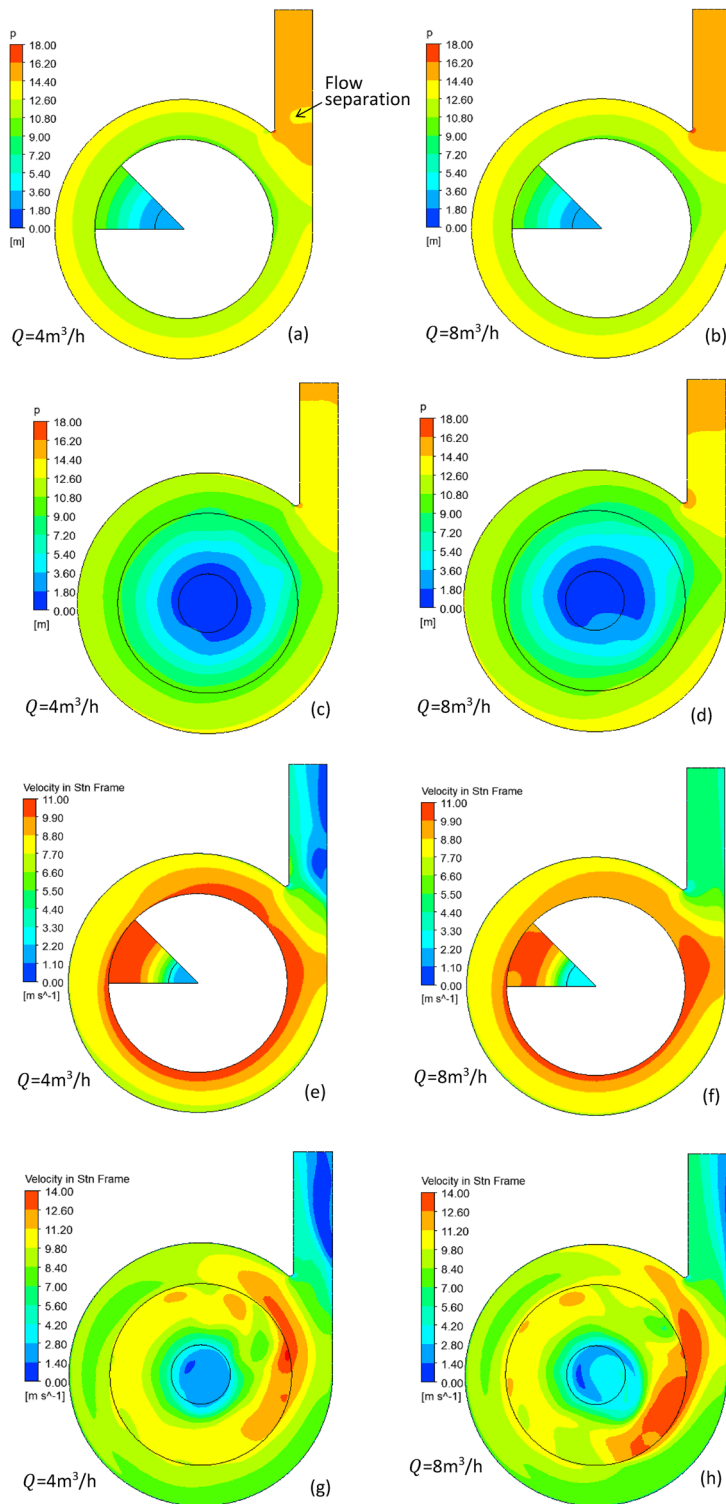


FIG. 13. Pressure and absolute velocity in mid-span plane of volute predicted with FRM at $Q = 4 \text{ m}^3/\text{h}$ (0.5BEP) and $8 \text{ m}^3/\text{h}$ (BEP): (a), (b), (e), and (f) results for fluid domains with periodical connection; (c), (d), (g), and (h) results for fluid domains without periodical connection. Stn—stationary.

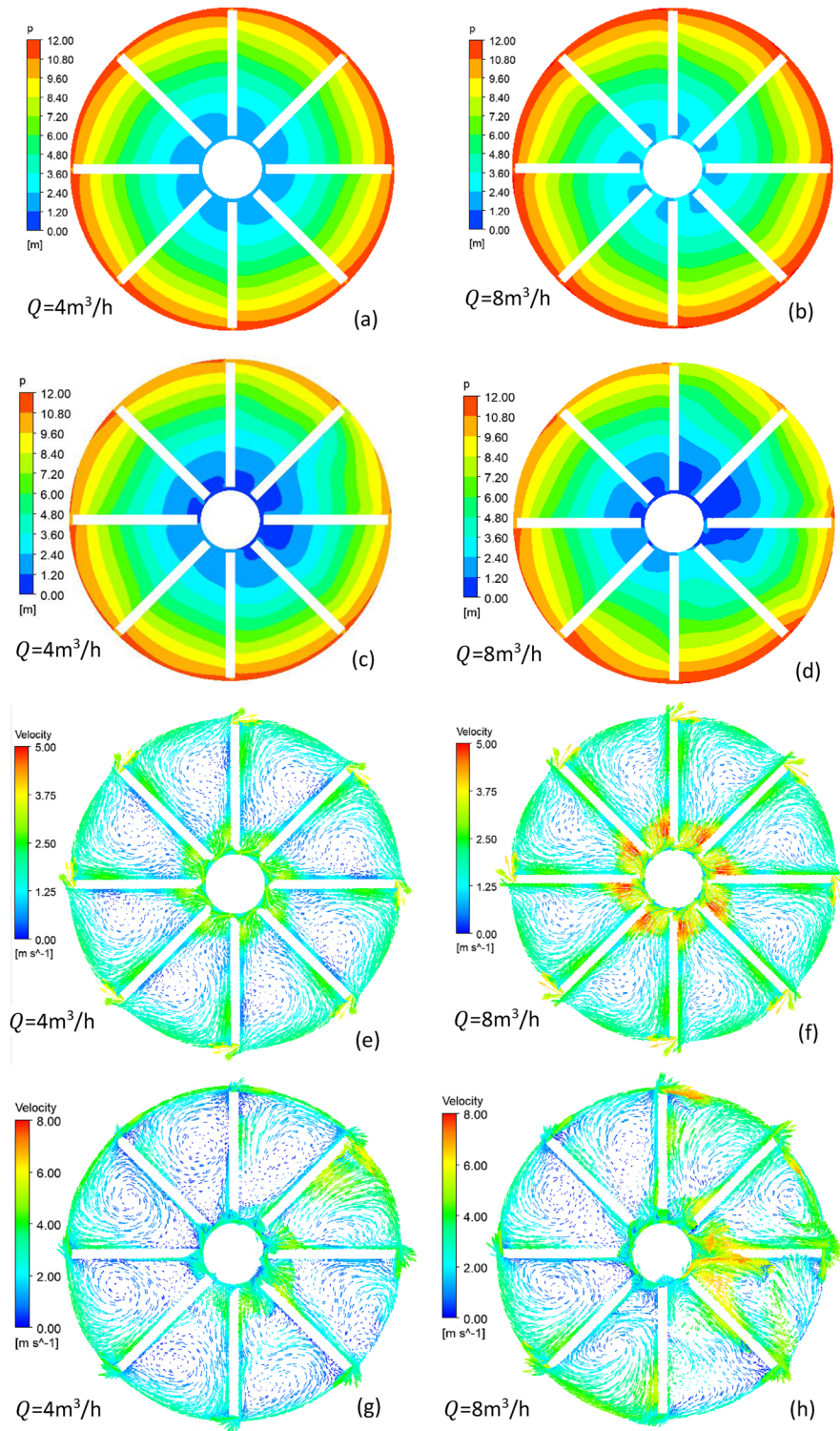


FIG. 14. Pressure distribution in mid-span plane of impeller predicted with FRM at $Q = 4 \text{ m}^3/\text{h}$ (0.5BEP) and $8 \text{ m}^3/\text{h}$ (BEP): (a), (b), (e), and (f) results for fluid domains with periodical connection, with seven flow passages duplicated from one flow passage; (c), (d), (g), and (h) results for fluid domains without periodical connection, where the velocity is the relative velocity of water in the impeller.

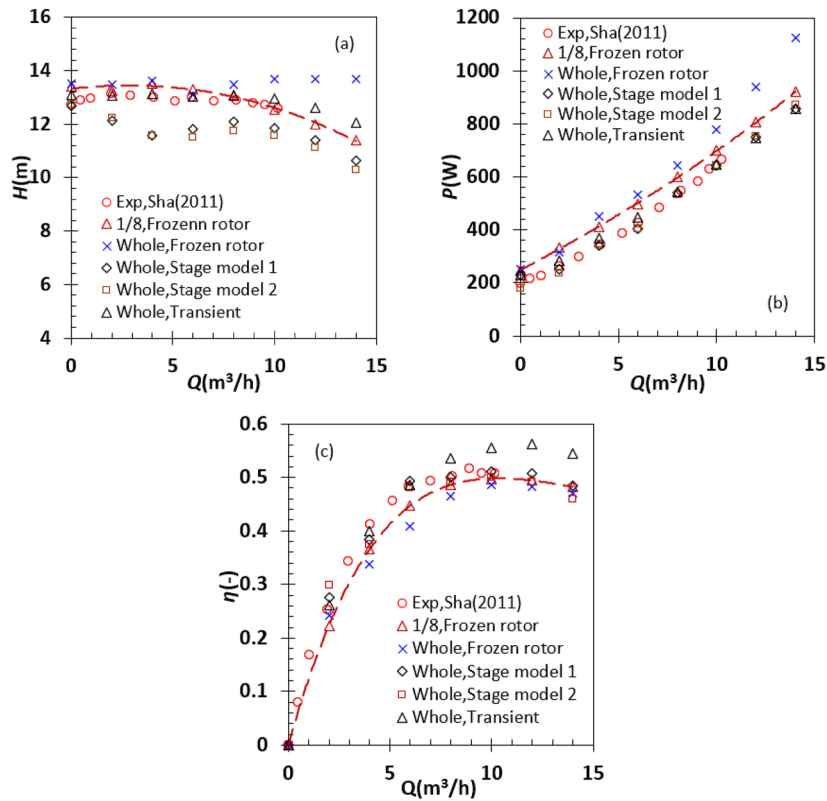


FIG. 15. Hydraulic performance of VP predicted by using FRM, SM, and TRM based on whole-impeller geometrical model: (a) head; (b) shaft power; (c) efficiency. Notes: 1/8–1/8-impeller geometrical model; Whole—whole-impeller geometrical model; SM 1—SM with constraint of downstream total pressure; SM 2—SM with constraint of downstream velocity; Transient—TRM.

$$\frac{P_d}{P} = \begin{cases} -0.0083 \left[\left(\frac{Re}{Re_w} \right)^{-0.5} \right]^2 + 0.2394 \left(\frac{Re}{Re_w} \right)^{-0.5} + 1.8731 \text{ at } 0.6\text{BEP}, \\ -0.0115 \left[\left(\frac{Re}{Re_w} \right)^{-0.5} \right]^2 + 0.2641 \left(\frac{Re}{Re_w} \right)^{-0.5} + 1.3477 \text{ at BEP}, \\ -0.0103 \left[\left(\frac{Re}{Re_w} \right)^{-0.5} \right]^2 + 0.2388 \left(\frac{Re}{Re_w} \right)^{-0.5} + 1.4322 \text{ at } 1.2\text{BEP}. \end{cases} \quad (14)$$

Furthermore, the ratio P_d/P for the centrifugal pump with a closed impeller at specific speed $n_s = 46.7$ in Ref. 62 is correlated with the impeller Reynolds number at BEP, and the corresponding correlation is

$$\frac{P_d}{P} = -10.4760 + 26.5750 \left(\frac{Re}{Re_w} \right)^{-0.2} \text{ at BEP} \quad (15)$$

The P_d/P curves calculated from Eqs. (14) and (15) at BEP are shown in Fig. 12(b). For the centrifugal pump with a closed impeller, the disc friction loss power ratio is 15% in water flow conditions, increasing to 55% with increasing viscosity. However, for the VP the ratio is less than 5%, and this suggests that the impeller disc friction loss power is a minor factor in reducing the efficiency of the VP.

C. Effect of periodical connection

In the fluid domains shown in Fig. 5(a), the pitch of the interface in the impeller fluid domain is 1/8 of that in the volute fluid domain. For the FRM in ANSYS CFX, the flow-variable profiles on the interface of the impeller fluid domain are scaled up to those on the interface of the volute fluid domain in the pitch-wise (circumferential) direction. The continuity, momentum, and turbulence model equations, among others, are scaled accordingly based on the pitch change.⁵³ This scaling process is akin to averaging or artificial mixing so that the flow variables are distributed more uniformly in the pitch-wise direction. The static pressure and absolute velocity of water in the mid-span plane of the vaneless chamber and the static pressure and relative velocity in the mid-span plane of the impeller at 0.5BEP ($Q = 4 \text{ m}^3/\text{h}$) and BEP ($Q = 8 \text{ m}^3/\text{h}$) are shown in Figs. 13 and 14, respectively. The inner part (the diameter of which is equal to the inner diameter of the suction pipe) and outer part (the diameter of which is in between those of the suction pipe and the volute) of the mid-span plane are upstream and downstream of the impeller, respectively.

As seen in Fig. 14, the pressure and flow in the mid-span plane of the impeller are axisymmetric in the fluid domains with periodical connection, but those in the domains with the whole impeller are not axisymmetric as shown in Fig. 13. Obviously, the pressure and

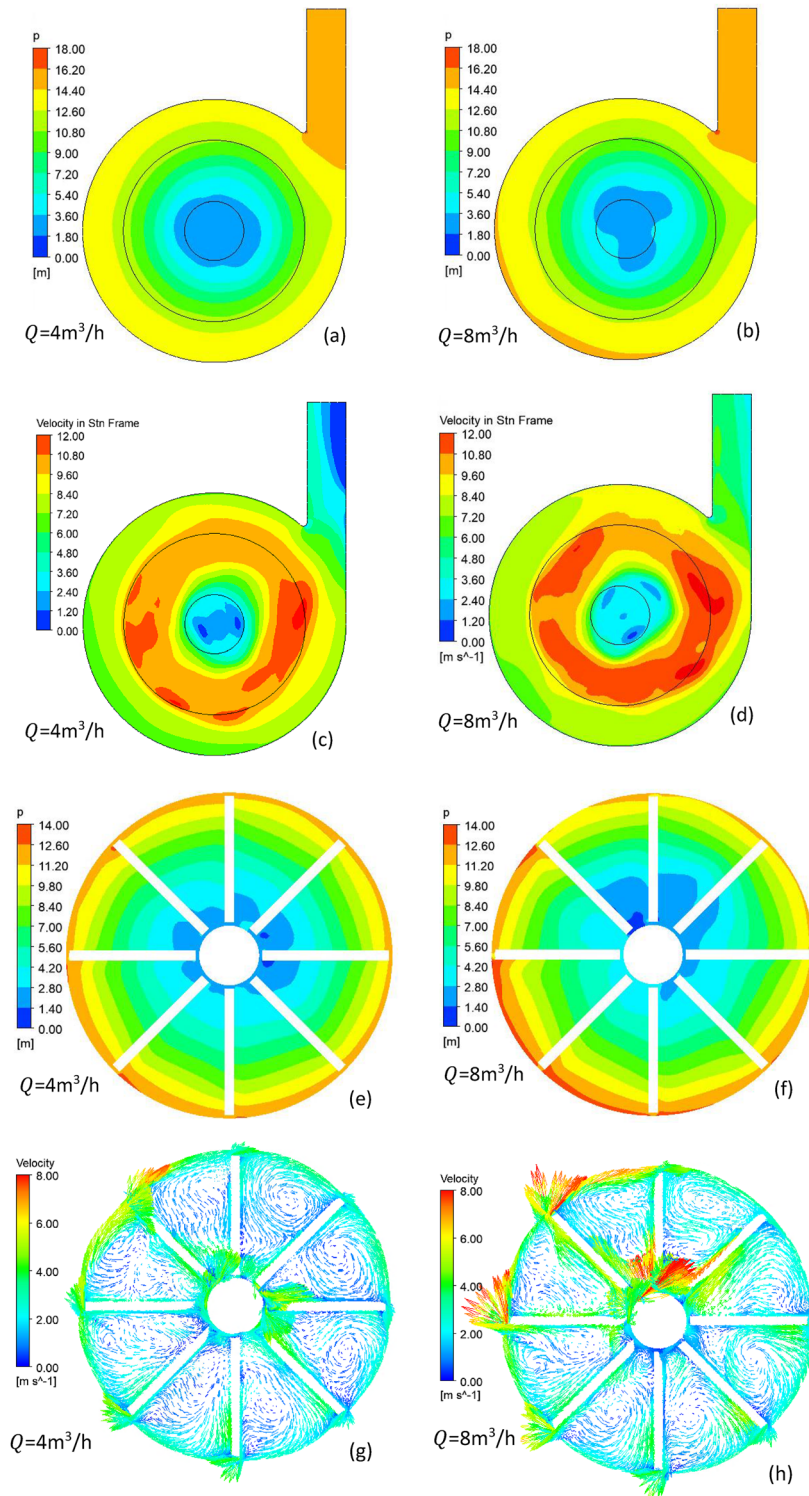


FIG. 16. Pressure distribution in mid-span plane of volute and relative velocity in mid-span plane of impeller predicted in fluid domains with whole-impeller based on TRM at $Q = 4 \text{ m}^3/\text{h}$ (0.5BEP) and $8 \text{ m}^3/\text{h}$ (BEP): (a)–(d) mid-span plane of volute; (e)–(h) mid-span plane of impeller, with velocity as the relative velocity of water in the impeller. Notes: (c) and (d) show the absolute velocity of water; Stn—stationary.

velocity are more uniform in the fluid domains with pitch change or periodical connection than in those with the whole impeller. As a result, the fluid flow experiences an artificial mixing process to reduce the head rise, and the predicted head is closer to the experimental measurement.

V. DISCUSSION

A. Novelty of present study

That the head curve predicted by CFD simulation is above the experimental head curve is common for VPs^{40,42,63–69} but the underlying reasons remain unclear. In the present study, this issue has been clarified in detail by using the CFD software ANSYS CFX 2019 R2, and the literature to date contains no such investigation into this phenomenon. Because the main focus in the present study was how the choice of interface model affects the hydraulic performance of a VP, other issues such as the vortex in the chamber, efficiency decomposition, slip factor, and hydraulic losses in the impeller and volute were not examined, and the interested reader should refer to Ref. 45 for those aspects.

B. Effects of three interface models for whole-impeller model

Three interface models were applied to the fluid domains with the whole impeller shown in Fig. 1 to identify the differences in their effects on the hydraulic performance curve from the corresponding effects on the performance curve based on the fluid domains with periodical connection. The predicted hydraulic performance curves based on the whole-impeller model by using the three interface models with mesh A are shown in Fig. 15. As can be seen, the FRM results in a significantly higher head and larger shaft power than the experimental data at over-load points ($Q \geq 8 \text{ m}^3/\text{h}$). The SM leads to considerably lower head and shaft power than the experimental values and so is unsuitable for the VP. The TRM produces a head that agrees with the experimental observation, but it also produces a smaller shaft power and thus a noticeably higher efficiency than the experimental efficiency at over-load points ($Q \geq 8 \text{ m}^3/\text{h}$). Overall, the effects of the SM and TRM on the performance in the fluid domain with the whole impeller resemble those in the domain with periodical connection.

Figure 16 shows the pressure and absolute velocity in the mid-span plane of the chamber and the pressure and relative velocity in the mid-span plane of the impeller as predicted by using the TRM in the fluid domains with the whole impeller for water. Compared with the pressure and absolute velocity in the chamber and the relative velocity in the impeller predicted by means of the FRM in Figs. 13 and 14, respectively, the pressure and flow pattern predicted with the TRM vary more uniformly in the circumferential direction, particularly at the part-load point.

The CFD simulations of turbulent flow in the VP reported herein were based on the standard $k-\epsilon$ two-equation model only, and wall roughness was not considered. Therefore, future work should consider other turbulence models and rough walls in the continued study of how the choice of interface model affects the hydraulic performance of the VP.

VIII. CONCLUSION

In the study reported herein, how the choice of interface model among the FRM, SM, and TRM affected the hydraulic performance of a VP with a specific speed of 76 and smooth walls in CFD simulations was investigated by using fluid domains with 1/8-impeller and whole-impeller geometrical models. Three-dimensional, steady, turbulent flows of water and viscous oils in the VP were simulated by using the Reynolds-averaged Navier–Stokes equations and the standard two-equation $k-\epsilon$ model as well as a scalable wall function in the CFD software ANSYS CFX 2019 R2. The influences of wall roughness and the whole-impeller geometrical model on the hydraulic performance were discussed.

The results showed that the head overestimation of the VP is related to using the FRM and the fluid domains with the whole-impeller geometrical model. If instead the 1/8-impeller model (periodical connection) and FRM are used, the predicted head of the pump is likely to agree well with the experimental observation. The TRM can predict a head that agrees well with the experimental head, but it requires huge computational resources and also overestimates the pump efficiency.

The flow patterns in the chamber and impeller predicted with the 1/8-impeller geometrical model were distributed more uniformly along the circumferential direction than were those predicted with the whole-impeller geometrical model by using the FRM, and the flow patterns predicted with the whole-impeller geometrical model by using the TRM were in between.

The hydraulic performance of the VP was predicted when pumping liquids with various kinematic viscosity in the 1/8-impeller geometrical model using the FRM, and the flow rate, head, and efficiency correction factors were obtained and correlated with the impeller Reynolds number.

ACKNOWLEDGMENTS

The author thanks the School of Engineering at the University of Glasgow, where the CFD simulations reported in this paper were conducted under a license for ANSYS CFX.

AUTHOR DECLARATIONS

Conflict of Interest

The authors have no conflicts to disclose.

Author Contributions

Wenguang Li: Conceptualization (lead); Data curation (lead); Investigation (lead); Methodology (lead); Software (lead); Validation (lead); Visualization (lead); Writing – original draft (lead); Writing – review & editing (lead).

DATA AVAILABILITY

The data that support the findings of this study are available from the corresponding author upon reasonable request.

REFERENCES

- ¹K. Rüttschi, "Die Arbeitsweise von freistrompumpen," *Schweiz. Bauztg* **86**(32), 575–582 (1968), <https://www.e-periodica.ch/cntmng?pid=sbz-002:1968:86::490>.
- ²H. Ohba, Y. Nakashima, K. Shiramoto, K. Shiramoto, and T. Kojima, "A study on internal flow and performance of a vortex pump: Part 2 A comparison between analyses and experimental results, and a design method of pump," *Bull. JSME* **26**(216), 1007–1013 (1983).
- ³G. P. Schivley and J. L. Dussourd, "An analytical and experimental study of a vortex pump," *J. Basic Eng.* **92**(4), 889–900 (1970).
- ⁴M. Aoki, "Studies on the vortex pump: 2nd report, pump performance," *Bull. JSME* **26**(213), 394–398 (1983).
- ⁵H. Ohba, Y. Nakashima, K. Shiramoto, K. Shiramoto, and T. Kozima, "A study on performance and internal flow pattern of a vortex pump," *Bull. JSME* **21**(162), 1741–1749 (1978).
- ⁶M. Aoki, "Studies on the vortex pump: 1st report, internal flow," *Bull. JSME* **26**(213), 387–393 (1983).
- ⁷M. Aoki, "Studies on the vortex pump: 3rd report, estimation of pump performance," *Bull. JSME* **26**(216), 1014–1019 (1983).
- ⁸H. Ohba, Y. Nakashima, K. Shiramoto, and K. Shiramoto, "On the performance of a vortex pump for solid-liquid fluid," *Turbomachinery* **10**(2), 76–82 (1982).
- ⁹V. Y. Kondus, R. V. Puzik, V. F. German, V. O. Panchenko, and S. M. Yakhnenko, "Improving the efficiency of the operating process of high specific speed torque-flow pumps by upgrading the flowing part design," in XVI International Scientific and Engineering Conference Hermetic Sealing, Vibration Reliability and Ecological Safety of Pump and Compressor Machinery, Sumy, Ukraine, 2020.
- ¹⁰Y. Sha and X. Liu, "Performance test on solid-liquid two-phase flow hydrotransport of vortex pump," *Trans. Chin. Soc. Agric. Eng.* **29**(22), 76–82 (2013).
- ¹¹K. Kikuyama, M. Murakami, K. Minemura, E. Asakura, and T. Ikegami, "The effects of entrained air upon a vortex pump performance," *Trans. Jpn. Soc. Mech. Eng., Ser. B* **52**(473), 393–400 (1986).
- ¹²Y. Sha and X. Liu, "Numerical calculation on gas-liquid two-phase hydrotransport and flow field measurement in volute with probes for vortex pump," *Trans. Chin. Soc. Agric. Eng.* **30**(18), 93–100 (2014).
- ¹³M. Yang, B. Gao, D. Liu, H. Li, and H. Gu, "Analysis on liquid-solid two-phase flow field in a vortex pump by PDPA measurement," *Trans. Chin. Soc. Agric. Mach* **38**(12), 53–57 (2007).
- ¹⁴M. Yang, B. Gao, D. Liu, H. Gu, and H. Li, "Experimental investigation of salt-out two-phase flow in a vortex pump by PDPA measurements," *J. Eng. Thermophys* **29**(2), 237–240 (2008).
- ¹⁵B. Gao and M. Yang, "Particle concentration distribution and its effect on salt-out features in a vortex pump," *J. Eng. Thermophys* **30**(12), 2031–2033 (2009).
- ¹⁶B. Gao and M. Yang, "Research on turbulent velocity fluctuations of salt-out particles in a vortex pump volute," *J. Eng. Thermophys* **31**(2), 275–278 (2010), <https://qikan.cqvip.com/Qikan/Article/Detail?id=32962965>.
- ¹⁷A. Gerlach, D. Perlitz, F. Lykholt-Ustrup, C. B. Jacobsen, and P. U. Thamsen, "The clogging behavior of a vortex pump—An experimental study on the influence of impeller designs," in The ASME 2017 Fluids Engineering Division Summer Meeting, Waikoloa, Hawaii, 2017.
- ¹⁸H. Ohba, Y. Nakashima, and K. Shiramoto, "A study on internal flow and performance of a vortex pump: Part 1 theoretical analysis," *Bull. JSME* **26**(216), 999–1006 (1983).
- ¹⁹H. Chen, "A study on internal flow field in a vortex pump," *Trans. Chin. Soc. Agric. Mach* **24**(2), 24–27 (1993), <https://qikan.cqvip.com/Qikan/Article/Detail?id=1132758>.
- ²⁰W. Shi, Y. Wang, F. Kong, Y. Sha, and H. Yuan, "Numerical simulation of internal flow field within the volute of vortex pump," *Trans. Chin. Soc. Agric. Eng.* **21**(9), 72–75 (2005).
- ²¹P. Xia, S. Liu, and Y. Wu, "Numerical simulation of steady flow in vortex pump," *J. Eng. Thermophys* **27**(5), 420–422 (2006).
- ²²W. Shi, Y. Wang, Y. Sha, H. Liu, and Z. Wang, "Research on the internal flow of vortex pump," *Trans. Chin. Soc. Agric. Eng.* **37**(1), 47–50 (2006).
- ²³M. Yang, B. Gao, H. Gu, and H. Li, "Measurement on 3D turbulent flow field in vortex pump," *Drain. Irrig. Mach* **26**(1), 60–63 (2008), <https://qikan.cqvip.com/Qikan/Article/Detail?id=26667331>.
- ²⁴Y. Sha, "Experiments on performance and internal flow of a vortex pump," *Trans. Chin. Soc. Agric. Eng.* **27**(4), 141–146 (2011).
- ²⁵M. Cervinka, "Computational study of sludge pump design with vortex impeller," in 18th International Conference on Engineering Mechanics, Svratka, Czech Republic, 2012.
- ²⁶J. V. Krishtop, P. M. Kalinichenko, and A. G. Gusak, "Calculation and designing of volutes of rotodynamic pumps," in XV International Scientific and Engineering Conference Hermetic Sealing, Vibration Reliability and Ecological Safety of Pump and Compressor Machinery, Sumy, Ukraine, 2017.
- ²⁷V. Kondus, P. Kalinichenko, and O. Gusak, "A method of designing of torque-flow pump impeller with curvilinear blade profile," *East-Eur. J. Enterp. Technol.* **3**(8(93)), 29–35 (2018).
- ²⁸H. Quan, Y. Chai, R. Li, and J. Guo, "Numerical simulation and experiment for study on internal flow pattern of vortex pump," *Eng. Comput.* **36**(5), 1579–1596 (2019).
- ²⁹H. Quan, Y. Chai, R. Li, G. Peng, and Y. Guo, "Influence of circulating-flow's geometric characters on energy transition of a vortex pump," *Eng. Comput.* **36**(9), 3122–3137 (2019).
- ³⁰L. Dai, L. Gu, J. Wang, X. Ao, and X. Zhu, "The effect of impeller indent distance on the performance of vortex pumps," *Int. J. Fluid Mach. Syst.* **13**(1), 42–54 (2020).
- ³¹H. Quan, J. Cheng, Y. Guo, L. Kang, and G. Peng, "Influence of screw centrifugal inducer on internal flow structure of vortex pump," *J. Fluids Eng.* **142**(9), 091203 (2020).
- ³²H. Quan, X. Yu, R. Li, K. Song, H. Pu, and W. Wang, "Influence of liquid viscosity on internal flow structure in vortex pumps," *J. Drain. Irrig. Mach. Eng.* **39**(12), 1278–1283 (2021).
- ³³K. Zhao, H. Liu, Z. Du, M. Tan, S. Hu, and L. Dong, "Analysis of flow loss characteristic of vortex pump based on entropy production," *J. Drain. Irrig. Mach. Eng.* **39**(12), 1284–1290 (2021).
- ³⁴A. Khayyaminejad, N. P. Khabazi, F. Gholami-Malek Abad, and S. Taheripour, "Numerical investigation on the effect of the geometric parameters of the impeller on vortex pump performance," *Iran. J. Sci. Technol.-Trans. Mech. Eng.* **47**, 1711–1731 (2023).
- ³⁵D. Zhang, M. Yang, B. Gao, and B. Lu, "Particle concentration distribution and its effect on performance in a vortex pump," *Fluid Mach* **42**(5), 22–25 (2013).
- ³⁶M. Yang, B. Gao, H. Li, and H. Gu, "Simulation and experimental research on salt-out two-phase flow field in a vortex pump," *Chin. J. Mech. Eng.* **44**(12), 42–48 (2008).
- ³⁷J. Qian, M. Yang, Y. Cao, B. Gao, and H. Wang, "CFD-PBM coupled calculation on liquid-solid two-phase flow field in a vortex pump," *Fluid Mach* **42**(4), 31–35 (2014).
- ³⁸D. Ye, H. Li, Q. Ma, Q. Han, and X. Sun, "Numerical investigation of performance improvement and erosion characteristics of vortex pump using particle model," *Shock Vib.* **2020**, 5103261.
- ³⁹Y. Imasaka, H. Kanno, S. Saito, K. Miyagawa, M. o Nohmi, M. Isono, and M. Kawai, "Clogging mechanisms of vortex pumps: Fibrous material motion capture and simulation with a CFD and DEM coupling method," in 5th Joint US-European Fluids Engineering Division Summer Meeting, Canada, Quebec, 2018.
- ⁴⁰J. Yuan, Z. Liu, R. Huang, L. Zhang, and D. He, "Investigation on energy conversion characteristics of vortex pump under bubble inflow," *CIESC J.* **74**(9), 3807–3820 (2023).
- ⁴¹D. H. He, G. Wang, Z. Liu, and R. Huang, "Bubble breakage and aggregation characteristics in a vortex pump under bubble inflow," *Phys. Fluids* **35**, 093301 (2023).
- ⁴²H. X. Chen, F. J. Shi, and J. H. Guo, "Numerical research on the three dimensional unsteady flow within the vortex pump," *Int. J. Turbo Jet Engines* **23**, 27–35 (2006).
- ⁴³A. Steinmann, H. Wurm, and A. Otto, "Numerical and experimental investigations of the unsteady cavitating flow in a vortex pump," in 9th International Conference on Hydrodynamics, Shanghai, China, 2010.
- ⁴⁴A. Gerlach, E. Preuss, P. U. Thamsen, and F. Lykholt-Ustrup, "Numerical simulations of the internal flow pattern of a vortex pump compared to the Hamel-Oseen vortex," *J. Mech. Sci. Technol.* **31**(4), 1711–1719 (2017).
- ⁴⁵W. Li and Y. Zhang, "The vortex pump under highly viscous liquid flow conditions," *Arabian J. Sci. Eng.* **43**(9), 4739–4761 (2018).

- ⁴⁶W. Li, “A mean-line flow model of viscous liquids in a vortex pump,” *Task Q* **26**(2), 1–18 (2022).
- ⁴⁷W. Li, “A CFD prediction of hydraulic and cavitation performance of a vortex pump as turbine,” *J. Xihua Univ., Nat. Sci. Ed.* **36**(1), 60–68 (2017).
- ⁴⁸W. Li, “Vortex pump as turbine—A type turbine for energy generation or recovery based on computational fluid dynamics prediction,” *J. Fluids Eng.* **141**(10), 1011051 (2019).
- ⁴⁹W. Li, “Vortex pump as turbine for energy recovery in viscous fluid flows with Reynolds number effect,” *J. Fluids Eng.* **144**(2), 021207 (2022).
- ⁵⁰Anonymous, FLUENT 6.2 User’s Guide, Volume1 and 2, Fluent Inc., Lebanon, NH 03766, 2005.
- ⁵¹F. M. White, *Viscous Fluid Flow*, 2nd ed., McGraw-Hill, Inc, New York, 1991.
- ⁵²Anonymous, ANSYS CFX-Solver Theory Guide, ANSYS, Inc., Southpointe, 2011.
- ⁵³Anonymous, ANSYS CFX-Solver Modeling Guide, ANSYS, Inc., Southpointe, 2011.
- ⁵⁴W. Li and Z. Hu, “Experiments on performance of a centrifugal highly viscous oil pump,” *Fluid Mach* **25**(2), 3–8 (1997), <https://qikan.cqvip.com/Qikan/Article/Detail?id=2635651>.
- ⁵⁵W. Li, F. Su, and C. Xiao, “Experimental investigations of performance of a commercial centrifugal oil pump,” *J. Fluids Eng.* **124**(2), 554–557 (2002).
- ⁵⁶W. Li, “Impeller trimming of an industrial centrifugal oil pump,” *Int. J. Adv. Des. Manuf. Technol* **5**(1), 1–10 (2011), <https://sanad.iau.ir/Journal/admt/Article/873083>.
- ⁵⁷T. Toyokura, J. Kurokawa, and T. Kanemoto, “Performance improvement of centrifugal pump for high viscosity liquid,” *Turbomachinery* **7**(2), 8–15 (1979).
- ⁵⁸T. Toyokura, T. Kanemoto, and K. Masuda, “Performance of non-clog type centrifugal pump using high viscosity liquid,” *Turbomachinery* **8**(2), 36–40 (1980).
- ⁵⁹A. Ladouani and A. Nemdili, “Development of new models of performance correction factors of centrifugal pumps as a function of Reynolds number and specific speed,” *Forsch. Ingenieurwes.* **77**, 59–69 (2013).
- ⁶⁰A. T. Ippen, “The influence of viscosity on centrifugal pump performance,” *Trans. ASME* **68**(8), 823–848 (1946).
- ⁶¹K. Aoki, T. Yamamoto, H. Ohta, and Y. Nakayama, “Study on centrifugal pump for high viscosity: Effect of impeller outlet angle on the pump performance,” *Trans. Jpn. Soc. Mech. Eng., Ser. B* **51**(468), 2753–2758 (1985).
- ⁶²R. Torabi and S. A. Nourbakhsh, “The effect of viscosity on performance of a low specific speed centrifugal pump,” *Int. J. Rotating Mach.* **2016**, 1.
- ⁶³P. Tan, Y. Sha, X. Bai, D. Tu, J. Ma, W. Huang, and Y. Fang, “A performance test and internal flow field simulation of a vortex pump,” *Appl. Sci.* **7**, 1273 (2017).
- ⁶⁴X. Gao, W. Shi, Y. Shi, H. Chang, and T. Zhao, “DEM-CFD simulation and experiments on the flow characteristics of particles in vortex pumps,” *Water* **12**, 2444 (2020).
- ⁶⁵X. Gao, T. Zhao, W. Shi, D. Zhang, Y. Shi, L. Zhou, and H. Chang, “Numerical investigation of an open-design vortex pump with different blade wrap angles of impeller,” *Processes* **8**, 1601 (2020).
- ⁶⁶S. Shen, M. Xue, and H. Zhou, “Analysis on unsteady pressure pulsation of inside vortex pump,” *Chin. Hydraul. Pneumatics* **6**, 97–102 (2020).
- ⁶⁷H. Quan, Y. Li, L. Kang, X. Yu, K. Song, and Y. Wu, “Influence of blade type on the flow structure of a vortex pump for solid-liquid two-phase flow,” *Machines* **9**, 353 (2021).
- ⁶⁸Z. Yin, Y. Gu, T. Fan, Z. Li, W. Wang, D. Wu, J. Mou, and S. Zheng, “Effect of the inclined part length of an inclined blade on the cavitation characteristics of vortex pumps,” *Machines* **11**, 21 (2022).
- ⁶⁹M. Tan, K. Zhao, X. Wu, H. Liu, C. Shao, and B. Pan, “Analysis on flow structure in a vortex pump under all flow rates,” *Water Supply* **23**(5), 1874 (2023).